Functionalization and Crosslinking of Reduced Graphene Oxide Sheets by Multiple Tetrazine Units to Improve the Energy Storage in Supercapacitors

Margarita Bosmi, Ademola Adeniji, Elise Michel, Arnaud Brosseau, Vitor P Brasiliense, Pierre Audebert, Remith Pongilat, Magali Gauthier, Fabien Miomandre

▶ To cite this version:

Margarita Bosmi, Ademola Adeniji, Elise Michel, Arnaud Brosseau, Vitor P Brasiliense, et al.. Functionalization and Crosslinking of Reduced Graphene Oxide Sheets by Multiple Tetrazine Units to Improve the Energy Storage in Supercapacitors. ChemElectroChem, In press, ⟨10.1002/celc.202300467⟩. ⟨hal-04324494⟩

HAL Id: hal-04324494
https://hal.science/hal-04324494v1

Submitted on 5 Dec 2023

ChemElectroChem

Research Article
doi.org/10.1002/celc.202300467

Chemistry Europe
European Chemical Societies Publishing

www.chemelectrochem.org

Functionalization and Crosslinking of Reduced Graphene Oxide Sheets by Multiple Tetrazine Units to Improve the Energy Storage in Supercapacitors

Margarita Bosmi,[a] Ademola Adeniji,[a, b] Elise Michel,[a] Arnaud Brosseau,[a] Vitor Brasiliense,[a] Pierre Audebert,[a] Remith Pongilat,[b] Magali Gauthier,[b] and Fabien Miomandre*[a]

A multi-tetrazine compound tailored for grafting on graphene sheets has been designed and investigated. It is composed of hydrogen substituted tetrazines involved in inverse Diels-Alder demand cycloaddition reactions for grafting and a central dialkoxytetrazine to confer redox properties to the final material. The successful incorporation of this compound in reduced graphene oxide was demonstrated by elemental analysis, XPS, Raman spectroscopy, AFM, SEM and XRD. Cyclic voltammetry shows the redox activity of the remaining central tetrazine unit in graphene and allows to assess the specific capacity of the material. A significant increase in the specific capacity was found compared to pristine graphene and another tetrazine model compound bearing only one grafting unit. This result was assigned to an increase in the specific area in relation to bridges created between graphene sheets, as evidenced by AFM and XRD. The performance in energy storage were assessed in symmetrical Swagelok cells confirming the high impact of the functionalization on capacitance values.

Introduction

Graphene is a one-atom-thick crystalline form of carbon in a two-dimensional hexagonal lattice which has known a huge boom since now fifteen years.[1,2] Apart from its application in various fields as sensors, electronics and so on, graphene has been envisioned as a very promising energy storage material in batteries[3] and supercapacitors.[4,5] However, to achieve good performance, one has to overcome several issues among which the processability, conductivity and exploitation of the huge theoretical specific area of graphene. Functionalization of graphene sheets is thus crucial for that goal.[6] Chemical functionalization of graphene sheets may prevent the agglomeration of graphene layers and, if well controlled, maintain the inherent properties of graphene, which is highy desired for applications. If one considers covalent grafting, most of the work in the literature relies on the functionalization of graphene oxide since it intrinsically contains a high number of organic functions. A reductive post-treatment is usually required to get a final material conductive enough to be used as an electrode. An alternative route consists in starting directly with a highly reduced graphene oxide which contains less defects and in introducing the new functions by using reactive species[7] or cycloaddition[8] among which Diels-Alder reactions take a large place.[9] Tetrazines are small aromatic electroactive compounds[10] which have proven their efficiency in inverse demand Diels Alder (IDDA) reactions[11,12] with now widespread application in the field of bioorthogonal derivatization.[13,14] Application of this reaction to graphene has been reported mostly by our group[15,16] and also very recently for luminescence application.[17]

In view of using the final graphene based composite as a charge storage material to be used in batteries or supercaps, people have focused their strategy on introducing either redox-active groups[18] or redox-active electrolytes.[19] Once again, most of the work was devoted in introducing various redox-active functions like quinones,[20,21] ferrocene[22] or metal complexes[23] on graphene oxide by covalent bonding to orginally present oxygenated functions through amine linkers. Introducing redox active group on highly reduced graphene oxide through cycloaddition is much more scarce[24] with a few examples relying on the diazonium derivatization.[25,26] If one comes back to the use of tetrazine as an efficient reagent in IDDA, unfortunately its transformation into pyridazine once grafted leads to the loss of the redox-active property. Therefore we are proposing a compound containing both tetrazine moieties to be grafted on reduced graphene oxide through IDDA and others remaining unreacted, thus still redox-active in the final material. Moreover, hydrogen terminated tetrazines have been recently demonstrated to be more reactive in IDDA than carbon substitued ones and therefore more easily incorporated into reduced graphene oxide.[27] The compound **2** below answers all these queries and offers the possibility of a

---

[a] Dr. M. Bosmi, A. Adeniji, E. Michel, A. Brosseau, Dr. V. Brasiliense,
Prof. P. Audebert, Prof. F. Miomandre
Université Paris-Saclay
Ecole Normale Supérieure Paris-Saclay, CNRS, PPSM
4 avenue des Sciences 91190 GIF-SUR-YVETTE (France)
E-mail: mioman@ens-paris-saclay.fr

[b] A. Adeniji, Dr. R. Pongilat, Dr. M. Gauthier
Université Paris-Saclay
CEA, CNRS, NIMBE
LEEL, 91191 GIF-SUR-YVETTE (France)

Supporting information for this article is available on the WWW under https://doi.org/10.1002/celc.202300467

double-end grafting which has proven to be efficient for bridging graphene oxide sheets in the case of a parent compound reacting by nucleophilic substitution.[28] Besides this cross-linking strategy has been shown as an efficient way to enhance the charge storage ability of the material through a large increase of the specific area.[29] Unfortunately, the nucleophilic substitution route requires the presence of oxygen rich functions on graphene which is detrimental for the material conductivity. Using IDDA as the bridging strategy opens the way of keeping the conductivity at a high level, increasing the specific area, while introducing redox active functions in the bridging unit for an enhanced storage.

This paper describes the synthesis and electrochemical properties of this new tetrazine derivative **Tz1** (see Scheme 1) on one hand and its covalent grafting on reduced graphene oxide as well as the properties of the resulting nanomaterial on the other hand. For comparison sake, another compound **Tz2** containing the same hydrogen ended tetrazine fragment for cycloaddition but no tetrazine in the resulting material have been investigated at the same time.

Results and discussion

Synthesis

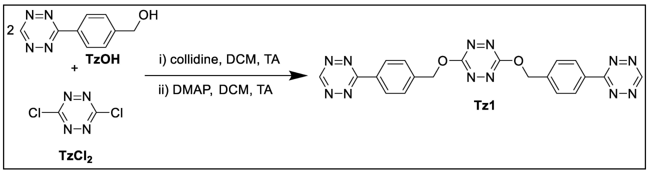

The syntheses of **TzOH** and **Tz2** have been reported in a previous paper.[30] The target compound **Tz1** is obtained in one step by a double nucleophilic substitution on dichlorotetrazine **$TzCl_2$** which is now commercially available with a final yield of 10% (see ESI for protocol details and NMR characterization).

Electrochemical properties of the molecules

The electrochemical features of **Tz1** in acetonitrile are shown in Figure 1 where they are compared with chloroethoxytetrazine (**ClTzOEt**) as a model compound (Figure 1a) and to **Tz2** (Figure 1b). **Tz1** displays an almost fully reversible redox peak in acetonitrile, but a shoulder and a much weaker reversibility in dichloroethane. The standard potential of **Tz1** is located at −1.08 V, i.e. 0.2 V more negative than **ClTzOEt**. This is typically the order of magnitude of the shift observed between chloroalkoxy and dialkoxy tetrazines.[10] Another significant difference between **Tz1** and **ClTzOEt** cyclic voltammograms is

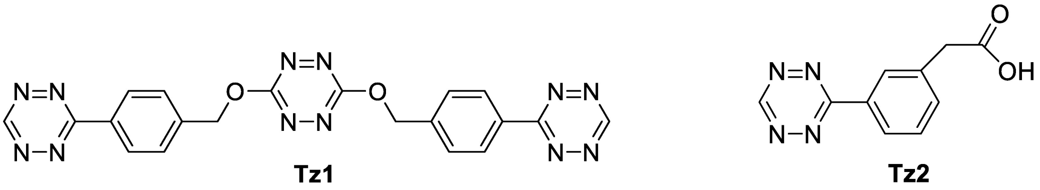

Tz1 **Tz2**

Scheme 1. Chemical formulas of the two hydrogen ended tetrazine derivatives investigated.

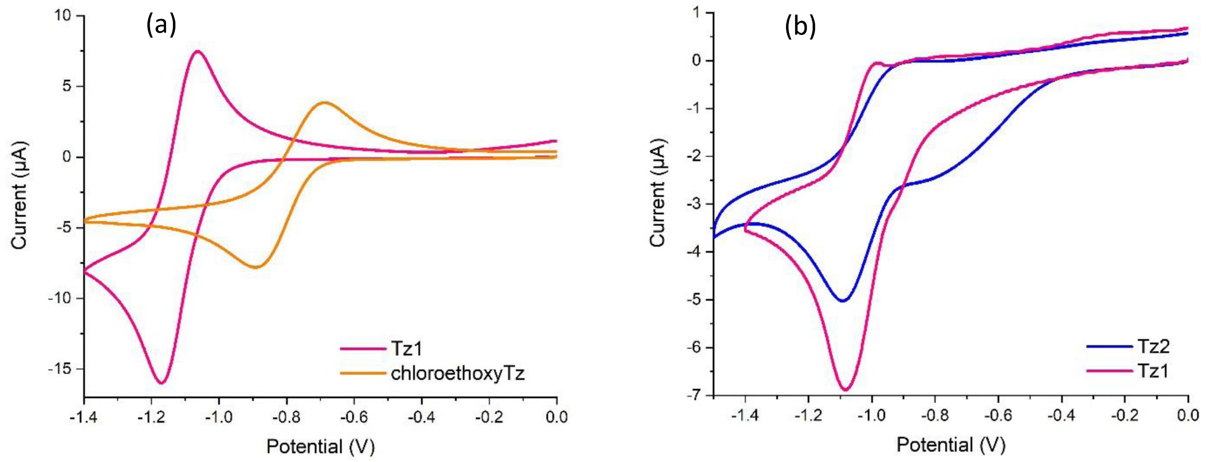

Figure 1. (a) Cyclic voltammograms of **Tz1** (pink trace) compared to chloroethoxytetrazine (orange trace) at the same scan rate (0.1 V/s) and same concentrations (1 mM) in acetonitrile (+$TBAPF_6$). (b) Cyclic voltammograms of **Tz1** (pink trace) and **Tz2** (blue trace) at the same concentration (0.5 mM in dichloroethane+$TBAPF_6$). Scan rate 0.1 V/s.

the reversibility of the signals, which is only partial in the former (the cathodic vs. anodic peak ratio is less than one). In a previous report, we demonstrated that hydrogen ended tetrazine can be reduced reversibly provided they do not contain an acidic function.[30] This means that the lack of reversibility in **Tz1** is due to the presence of three redox units, leading to a three times charged species for its fully reduced form. Moreover, the reversibility increases with the scan rate, showing that a chemical reaction follows the electron transfer (see Figure S1). Here the three times charged species generated by the reduction of **Tz1** behaves as a rather strong base likely to react with traces of water in the solvent. The signal becomes almost irreversible in dichloroethane.

The assignment of the reduction peaks of **Tz1** in dichloroethane can be deciphered by the comparison with **Tz2** which contains only hydrogen ended tetrazines and that displays the same reduction peak located at the same potential. Thus, the main peak is due to the hydrogen ended tetrazines and the shoulder to the central tetrazine ring. The broad and ill-defined reduction peak observed in **Tz2** around -0.7 V is due to the reduction of protons of the benzoic acid moiety.

The number of tetrazines involved in the reduction signal of **Tz1** was assessed by calibration vs. the reference compound **ClTzOEt**, using the following equation based on the Randles-Sevčik relationship (1):

$$\frac{n}{n_{ref}}=\frac{\alpha}{\alpha_{ref}}\frac{\sqrt{D_{ref}}}{\sqrt{D}}=\frac{\alpha}{\alpha_{ref}}\frac{\sqrt{R}}{\sqrt{R_{ref}}} \qquad (1)$$

where n is the number of electrons exchanged, D is the diffusion coefficient, R is the molecular radius and α is the slope of the current vs. square root of scan rate relationship (Randles slope).

Molecular modelling and energy minimization allow us to coarsely estimate the radius of each compound (see Figure 2) and leads to a square root of radius ratio of 1.17. The Randles slope ratio $\frac{\alpha}{\alpha_{ref}}$ being equal to 2.0 (see Figure S2), this leads to $\frac{n}{n_{ref}}=2.34$. This is result is not the expected value but the calculation relies on the assumption that no geometrical reorganization occurs after each electron uptake which is maybe not exact. Moreover, the solvation may vary as well and this parameter is not taken into account in the size determination from molecular modelling.

The same comparison of the peak current between **Tz1** and **Tz2** in dichloroethane is also consistent with the fact that all tetrazine units in **Tz1** are electroactive and display a single redox peak.

Synthesis and characterization of the functionalized materials

Grafting of **Tz1** and **Tz2** on reduced graphene oxide has been performed according to a procedure already reported by us.[15] To measure the material's capacitance a previously established protocol reported by Dong et al[31] was followed (see experimental section for details).

The expected final structures are very different for both materials as represented in Scheme 2. Whereas **Tz1** may act as a bridging redox active unit, **Tz2** is likely to simply functionalize the graphene sheets with non-electroactive functions. The following characterizations aim to demonstrate if these structures are actually obtained and what is the impact on the electrochemical storage in supercapacitors.

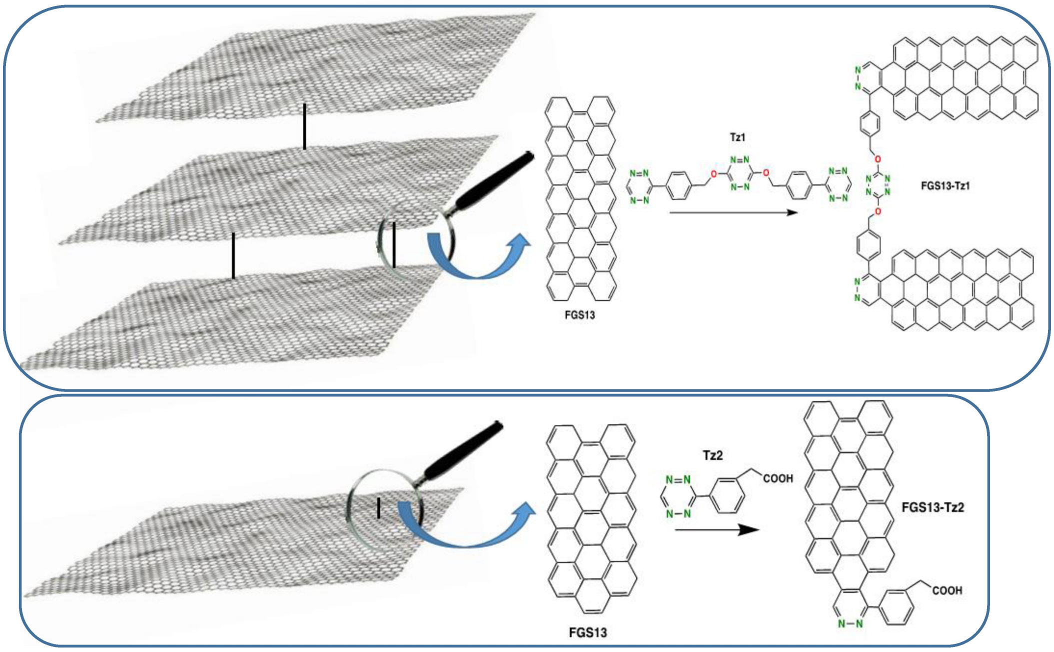

Scheme 2. Functionalization of graphene sheets in **FGS13** by **Tz1** (top) and **Tz2** (bottom).

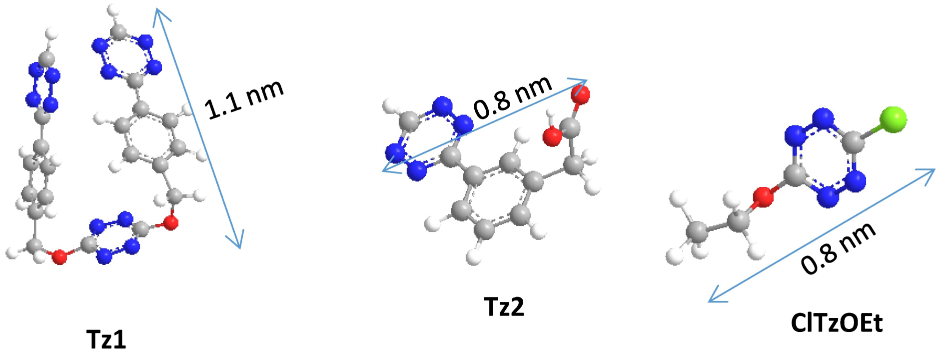

Figure 2. Representation and estimated sizes of the molecules after energy minimization and molecular dynamics running Chem3D.

Elemental analysis

Elemental analysis (EA) has been performed to check the presence of tetrazine in the final material. The elemental composition results are shown in table 1.

Two types of pristine graphene materials have been investigated: FGS13 and commercial reduced graphene oxide (SA). The results clearly show the presence of nitrogen in all grafted materials, as well as an increase in the amount of hydrogen, which is more sensitive in the case of **Tz1** as expected: indeed, based on the molecular hydrogen content, the ratio of additional hydrogen amounts between grafted and pristine materials should be nearly twice for **Tz1** vs. **Tz2**. The amount of nitrogen is about twice in **Tz1** compared to **Tz2**, which is less than expected if one considers that the central tetrazine ring remains intact and the hydrogen ended ones loose two nitrogen atoms each at the end. This is not surprising since tetrazine is known to decompose very easily into N_2 upon heating leading to an underestimation of the real nitrogen content in the material.

Table 1. Elemental composition of the various materials: SA = commercial (Sigma Aldrich) reduced graphene oxide; FGS13 = Functionalized Graphene Sheet with C/O ≈ 13.

	SA	SA-Tz1	SA-Tz2	FGS13	FGS13-Tz1
%C	98.3	90.9	90.5	73.4	69.4
%H	0.10	0.26	0.19	0.70	1.13
%N	0.00	0.54	0.26	0.00	0.68

X-ray Photoelectron Spectroscopy

The XPS spectra of the pristine **FGS13** and grafted **FGS13-Tz** compounds are shown in Figure 3 – Figure S3. The resulting elemental composition of each compound is shown in Table 2. The starting graphene that was used in this study is supposed to have a C/O ratio of about 13 (FGS 13). However, XPS revealed an excess of O probably coming from the underlying ITO substrate, as pristine graphene is difficult to coat on ITO. This is not the case with the **FGS-Tz** compounds that are easier to disperse and adhere more on ITO and thus shows an appropriate C/O ratio. After grafting by tetrazine derivatives, a new signal appears in the XPS spectra of **FGS13-Tz** near 400 eV corresponding to N 1s (Figure 3). The increase in the amount of carbon and the decrease of oxygen is also an indication of the tetrazine grafting.

Table 2. Atomic percentages in pristine **FGS13** and **FGS13-Tz** with various amounts of tetrazine (2Tz = twice amount of Tz as reactant) determined by XPS. Similar data obtained by replacing **FGS13** by commercial reduced graphene oxide (SA).

Sample	%C	%N	%O
FGS13	78.8 (96.0)*	0.3 (0.1)*	20.9 (3.5)*
FGS13-Tz1 (120 °C)	92.6	1.15	6.2
FGS13-2Tz1 (140 °C)	85.5	1.1	13.4
FGS13-Tz2 (120 °C)	92.6	0.5	6.7
FGS13-2Tz2 (140 °C)	86.3	0.5	13.1
SA	96.5	0	3.5
SA-Tz1 (120 °C)	92.8	1.1	5.6
SA-Tz2 (120 °C)	77.2	0.4	22.4

*Values measured on powder.

When we examine in more detail the signal of each element, we can assign the different contributions to different types of carbon and nitrogen. For **FGS13** (Figure S3a), we have a main peak of sp^2 and sp^3 aromatic carbons (284.7 eV), the **C**–O–C epoxy ring and the **C**–OH peak (286 eV), the **C**=O peak (287.3 eV) and the carboxyl functional groups at 288.9 eV, which agrees with previous spectroscopy measurements on reduced graphene oxide.[28,32]

For **FGS13-Tz1** and **FGS13-Tz2**, the main contributions are in the same area and the peaks at 287.9 eV can either be attributed to the tetrazine ring or to the carboxylic acid function (see Figure 3a,c). The contribution of this peak is larger for **FGS13-Tz1** as expected because the functionalization has worked better in the case of **Tz1**. For **FGS13-Tz1**, the N 1s signal (see Figure 3b) shows the pyridazine signal at 399.9 eV and a second contribution at 401 eV which can be assigned to the tetrazine ring.[15] The two distinct bands are typical of tetrazine functionalized material and might be due to specific interac-

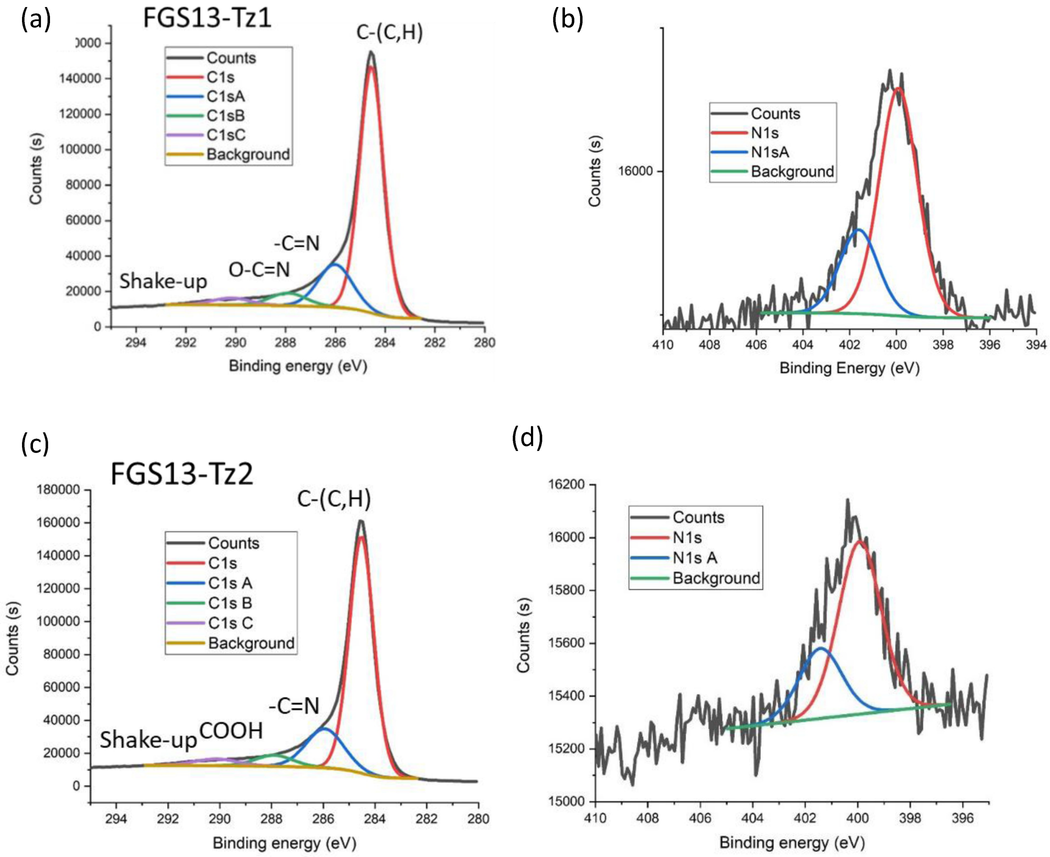

Figure 3. XPS spectra of **FGS13-Tz1**(a,b) and **FGS13-Tz2** (c,d): C 1s (a,c) and N 1s (b,d) curve fitting results. Assignments of the various C1s peaks (A–C) are indicated in the figure (highest energy C1sC in is a shake-up signal). The N signal contains two contributions named N1s and N1sA, see text for their respective assignments.

tions (like hydrogen bonding) between the nitrogen atoms of the tetrazine ring that are closer to the graphene sheets and the functionalities in the vicinity (carboxylic acids). The same peaks are recorded also for **FGS13-Tz2** (Figure 3d).

The XPS spectra of commercial graphene (**SA**) were also analysed for comparison. As shown in Figure S4, a similar behaviour as for **FGS13** can be seen. When we analyse in more detail the C 1s signal for pristine SA (Figure S4C), we see fewer contributions than for **FGS13**. This is expected as **SA** has less oxygen than **FGS13** and therefore contains less functional groups. More precisely, we can see only two main contributions, one corresponding to sp^2 and sp^3 aromatic carbons at 284.7 eV and one that corresponds to the **C**–O–C epoxy ring and the **C**–OH peak at 286 eV. For **SA-Tz1** (Figure S4), two new contributions for the carbon signal appear. The first one at 287 eV is assigned to the C=N signal in pyridazine units formed after cycloaddition and the second one at higher energy (289 eV) proves the presence of more oxidized groups and corresponds to the middle tetrazine function of **Tz1**, more precisely the O–C=N group. This result agrees well with our hypothesis that the hydrogen ended tetrazines of the molecule are the ones taking part to the inverse demand Diels-Alder reaction while the one in the middle remains unreacted.

Table 2 shows that the nitrogen amount is still twice in **FGS13-Tz1** relatively to **FGS13-Tz2** as in the elemental analysis and that the tetrazine compound is already in large excess in **FGS13-Tz1** as doubling the amount does not change the final nitrogen content (see **FGS13-2Tz1**). The same conclusion can be drawn for the second material **FGS13-Tz2**. Finally, the amount of nitrogen in the final material is similar for both types of graphene (**FGS13** and **SA**).

Electrochemistry

Figure 4 shows the cyclic voltammograms of the grafted materials coated on ITO overlaid with those of the corresponding precursor in solution. In the case of **FGS13-Tz1**, the presence of tetrazine in the grafted material is evidenced by a redox peak located at ca. −1.2 V, which is not present in the pristine graphene and appears slightly negatively shifted compared to the precursor **Tz1** (see Figure 4a). Moreover, the redox signal is reversible, which is expected for the reduction of a dialkoxytetrazine[33] and makes it distinguished from the reduction of other functions likely to be present in reduced graphene oxide. This shows that the electroactivity of the central tetrazine in **Tz1** remains intact in the functionalized material, as expected in the structure of Scheme 2. One can also notice the increase in the capacitive current when comparing **Tz1** and **FGS13-Tz1**, but also from **FGS13** to **FGS13-Tz1**, related

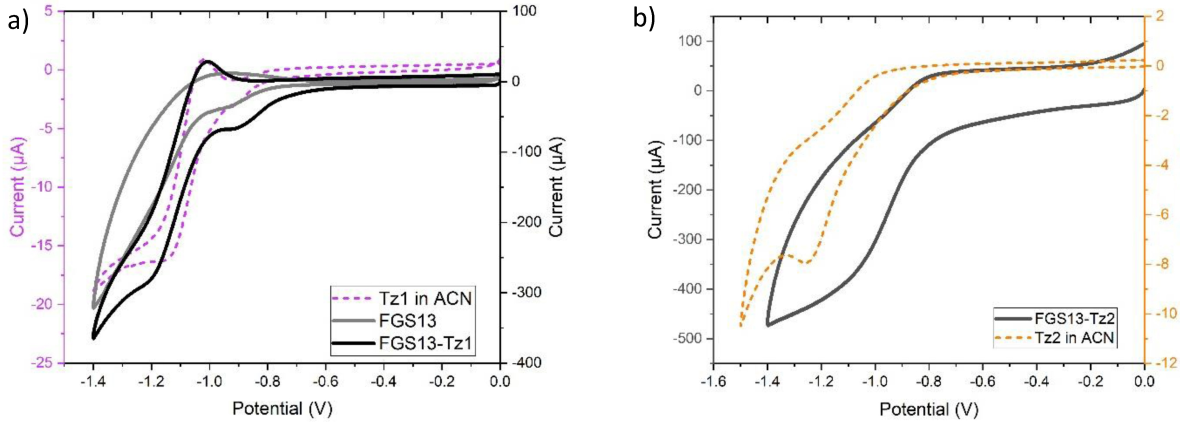

Figure 4. a) Cyclic voltammograms of **Tz1** in solution (purple line), **FGS13** on ITO (black line) and **FGS13-Tz1** coated on ITO (gray line). Scan rate 0.005 V/s. b) Cyclic voltammograms of **Tz2** (orange dashed line) 1 mM in ACN vs. **FGS13-Tz2** (black full line) coated on ITO from suspensions (ca. 1 mg/mL). Scan rate 0.1 V/s.

to an increase in the specific area of the material. Figure 4b shows the same comparison for **Tz2** and **FGS13-Tz2**. This time, a reduction peak is hardly visible in **FGS13-Tz2** and the measured current is mostly capacitive, as expected due to the fact that most tetrazine units in **Tz2** did react upon grafting and thus become inactive in the final material (see Scheme 2).

The difference between the cyclic voltammograms of **FGS13-Tz1** and **FGS13** can provide a rough estimation of the number of redox active tetrazine units in the final material. By integrating the surface of the reduction peak, we can estimate the total amount of charge and therefore deduce the number of moles of tetrazine from Faraday's law. Albeit difficult to measure precisely due to the graphene contribution, the charge found for the tetrazine reduction is estimated to ca. 5 mC.

From the XPS measurements, we found that the nitrogen amount in the functionalized material is 1,15 %. The number of moles corresponding to this percentage can be calculated by dividing it by the molecular weight of carbon (assimilating graphene to pure carbon in first approximation) and then by the number of nitrogen atoms present in the molecule once grafted (8 if we assume that both end groups contribute). This leads as to the following result:

$n(Tz1) = (\%N)/8/12 \approx 1.5\ \ 10^{-4}$ moles per gram of graphene.

As 100 μg was deposited on ITO to do the CV, the corresponding amount of grafted tetrazine is equal to 15 nmol, which should lead to a charge of 1.5 mC. The order of magnitude found is thus consistent with the estimation directly drawn from CV in Figure 4a.

Raman spectroscopy

We further confirm the functionalization of the surfaces by analysis of the Raman spectra of pristine and functionalized graphene samples. Raman spectroscopy is a powerful tool for characterizing graphene samples, enabling scrutinization of samples bearing different density of defects,[34–39] number of stacked layers,[37] among many other characteristics. In the context of surface modification and crosslinking of graphene, two metrics are of particular interest: (i) the ratio between the D (~1350 cm^{-1}) and G (~1587 cm^{-1}) bands, which has been shown to reflect the average number of defects present in the sp^2 structure;[35–37] and (ii) the position of the G (~1587 cm^{-1}) band, which is correlated to the average number of layers.[38]

We thus expect that functionalization of graphene samples with the bifunctional tetrazine linker **Tz1** should lead to both an increase of the I_D/I_G ratio, due to the addition of a pyridazine unit on the sp^2 backbone[35–37] and to a shift of the G band position towards lower wavenumbers, due to the crosslinking (and thus stacking) of many graphene layers.[38] Such effects were difficult to observe on **FGS13**, as its initially high density of defects (due to the many present functional groups) already displayed a strong I_D/I_G ratio (Figure S5). Instead, the comparative analysis was performed on high quality commercial graphene **SA**, which contained a low density of defects, for which subtle effects were more easily analysed. We account for the effect of the functionalization treatment by comparing graphene samples functionalized with **Tz1** with a control group having been subjected to the same functionalization procedure but omitting the tetrazine. Superposition of the recorded spectra is shown in Figure 5A, where a large number of graphene flakes is evaluated to avoid artefacts associated with the sample heterogeneity. A more detailed analysis of the spectra can be achieved by fitting the Raman bands, leading to the histograms shown in Figures 5B and 5C. Functionalization of graphene with **Tz1** leads to the expected enhancement of the I_D/I_G ratio (Figure 5B), which significantly evolves from the initial value of 0.15 ± 0.03 (3σ error) to 0.25 ± 0.04. Such observation indeed indicates an increase in defect density, suggesting that the tetrazine functionalization induces the formation of sp^3 defects in the conjugated sp^2 backbone. These conclusions are further supported by observing the position of the G band (Figure 5C), which shifts from a distribution centred on 1586.9 ± 0.3 cm^{-1}, compatible with single layer graphene, to 1583.7 ± 0.4 cm^{-1}. Estimation of the number of layers using the

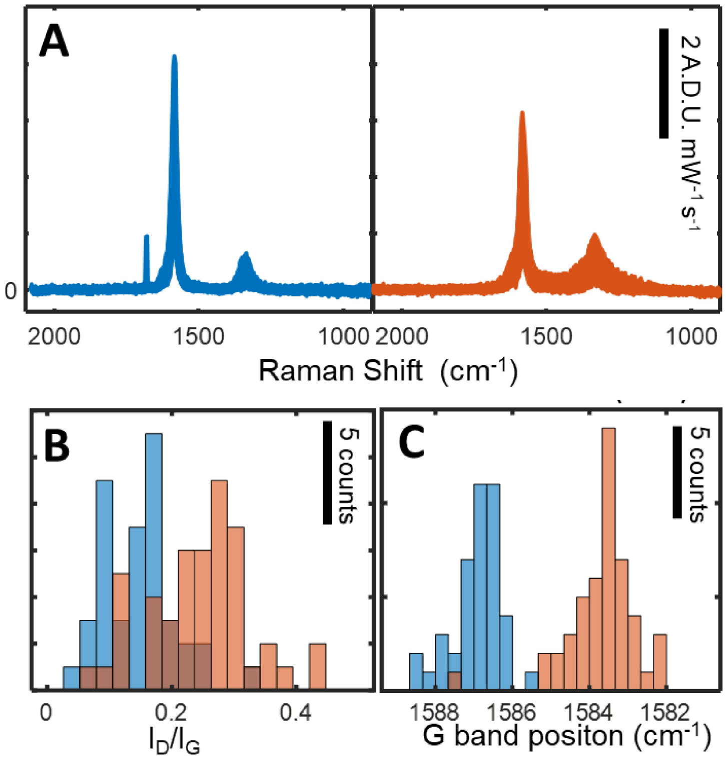

Figure 5. (A) Superposition of Raman spectra of commercial graphene flakes subject to the same functionalization treatment in the absence (blue, N = 42 probed zones) and presence (orange, N = 48 probed zones) of **Tz1** linkers. (B) Histogram showing the distribution of the relative intensity of the D and G bands, indicating significant increase of the I_D/I_G ratio. (C) Histogram summarizing the G band position, supporting an increase in the number of stacked graphene layers, as expected for crosslinking of samples through the **Tz1** linker.

empirical relation given in ref.[38] yields between 2 and 4 layers if lattice strain effects are neglected. We note that measurement of graphene thickness can be influenced by other factors such as strain, charging and doping;[39] however, taken together, our observations clearly support **Tz1** induced formation of covalent bonds between graphene layers, consistently with the structure hypothesized in Scheme 2.

Atomic force microscopy

Atomic force microscopy (AFM) is a common technique to study the topography of graphene's surface. The high resolution that can be achieved with AFM is useful when we want to examine separate sheets and measure their thickness. In our case, AFM was used to better understand the morphology of the functionalized graphene sheets and compare the mean thickness of the objects found in our two functionalized samples, **FGS13-Tz1** and **FGS13-Tz2**.

In order to have a clear image for the majority of functionalized graphene, we investigated different areas of the dispersion deposited on a silicon wafer. In most areas, pristine graphene remains in blocks and small aggregations which are not easy to disperse (see Figure S6). In the areas that are better dispersed we can find isolated graphene sheets and measure their thickness. AFM has revealed in the past the morphology of FGS_x and the typical thickness of a graphene sheet is around 2 nm.[28] A similar pattern can be seen for **FGS13-Tz2** as shown in Figure 6a with a thickness around 7 nm for graphene particles, but divided into sheet packs of 2 nm. There are also some areas where bigger objects were found and are probably packs of graphene sheets that have not been functionalized or have been after restacking (Figure S6B). This also explains the small percentage of functionalization for **FGS13-Tz2**. Conversely, **FGS13-Tz1** shows in the majority of its surface much thicker tacked objects with thickness up to 1.2 μm (Figure 6b). This result is consistent with the bridging of sheets which are maintained together through the cycloaddition of the hydrogen ended tetrazine units (see Scheme 2). It is important to note that we also observe some objects of smaller thickness that probably correspond to agglomerated unreacted graphene sheets (Figure S6C). However, the AFM images and thickness profiles shown in Figure 6 can be considered as representative of most of what is found in **FGS13-Tz1** and **FGS13-Tz2**.

SEM and XRD

Here, we use the combination of SEM and XRD techniques to have insight into the structural properties of **FGS13** and **FGS13-Tz1** to further confirm the hypothesized structure of Scheme 2. The results obtained are shown in Figure 7A and are in line with our expectations. Indeed, **FGS13** exhibits thin flake-like sheets of layered structure that are loosely packed (compared to

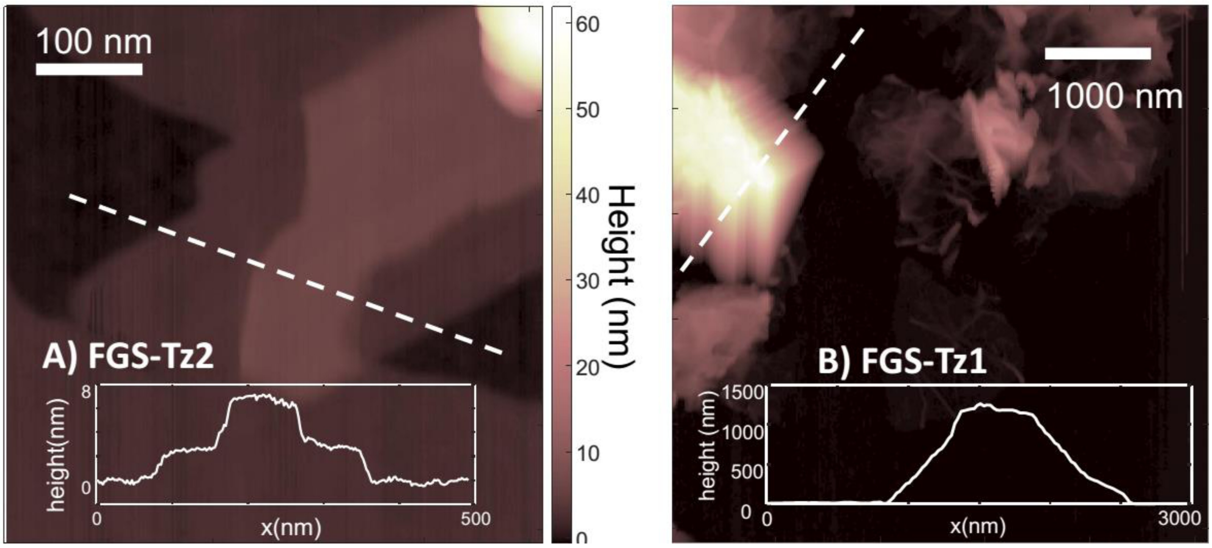

Figure 6. AFM images and thickness profiles of (A) **FGS-Tz2** and (B) **FGS-Tz1**.

graphite), typical of reduced graphene oxide produced through the rapid thermal exfoliation of graphene oxide. SEM micrographs reveal that **FGS13-Tz1** exhibits a layered structure with noticeable defects, pore holes, and enhanced interlayer spacing compared to the pristine sample.

Further analysis with XRD revealed an interesting result: **FGS13-Tz1** exhibits a larger broad peak area around 26° compared to the pristine material (see Figure 7B), indicating a decrease in crystalline size. Moreover, a new peak at $2\theta = 44°$ typical of nitrogen doped graphene[40,41] was observed, indicating the presence of a new structural orientation after functionalization.

The interlayer spacing measurements at $2\theta = 26°$ and 44° corresponding to planes (002) and (100), respectively, were found to be 0.342 nm and 0.206 nm for **FGS13-Tz1**, compared to 0.336 nm at $2\theta = 26.5°$ in the case of the pristine sample. These results further support the SEM observations of enhanced interlayer spacing in the functionalized sample.

Capacitance measurements

Functionalization with **Tz1** proved to be efficient at creating covalent bridges between graphene sheets through cycloaddition of the hydrogen ended tetrazine units. This linkage between the sheets prevents them from restacking back to graphite and therefore should increase the final specific area. Therefore, we expect that the capacitance of graphene is increased after functionalization.

Three-electrode cell

A first set of experiments were carried out in a three electrode cell where the working electrode potential is monitored vs. a reference. Classical cyclic voltammograms are obtained from which the capacitance can be assessed using relation (2) which correlates the capacitive current with the scan rate *v* in the potential window where no redox reaction occurs (pure capacitive behavior). The results are shown in Figure 8 and table 3.

$$i_{cap}(t) = C\frac{dE}{dt} = Cv \qquad (2)$$

The capacitive current was measured vs. the scan rate for **FGS13-Tz**1 and **FGS13-Tz2** and the results are shown in Figure S7. From the slopes of the straight lines obtained, we can extract the specific capacitance of the material and divide it by the graphene mass to obtain the specific capacitance values reported in Table 3. We notice a significant increase in the capacitance of **FGS13** after functionalization with **Tz1** and also higher values compared to **FGS-Tz2**. This is expected because of the increase of the specific area of graphene after bridging the sheets with **Tz1**, which does not occur with **Tz2**.

Two-electrode Swagelok cells

Capacitance measurements were also performed in two-electrode symmetrical Swagelok cells after depositing the active material (80%wt) in presence of PVDF binder (10%wt) and conductive carbon (10%wt) on aluminium substrates (see

Table 3. Capacitance values extracted from the capacitive current vs scan rate on modified ITO.

Sample	Capacitance (F/g)	
	without PVDF	with PVDF
FGS13-Tz1	20	26
FGS13-Tz2	12	14

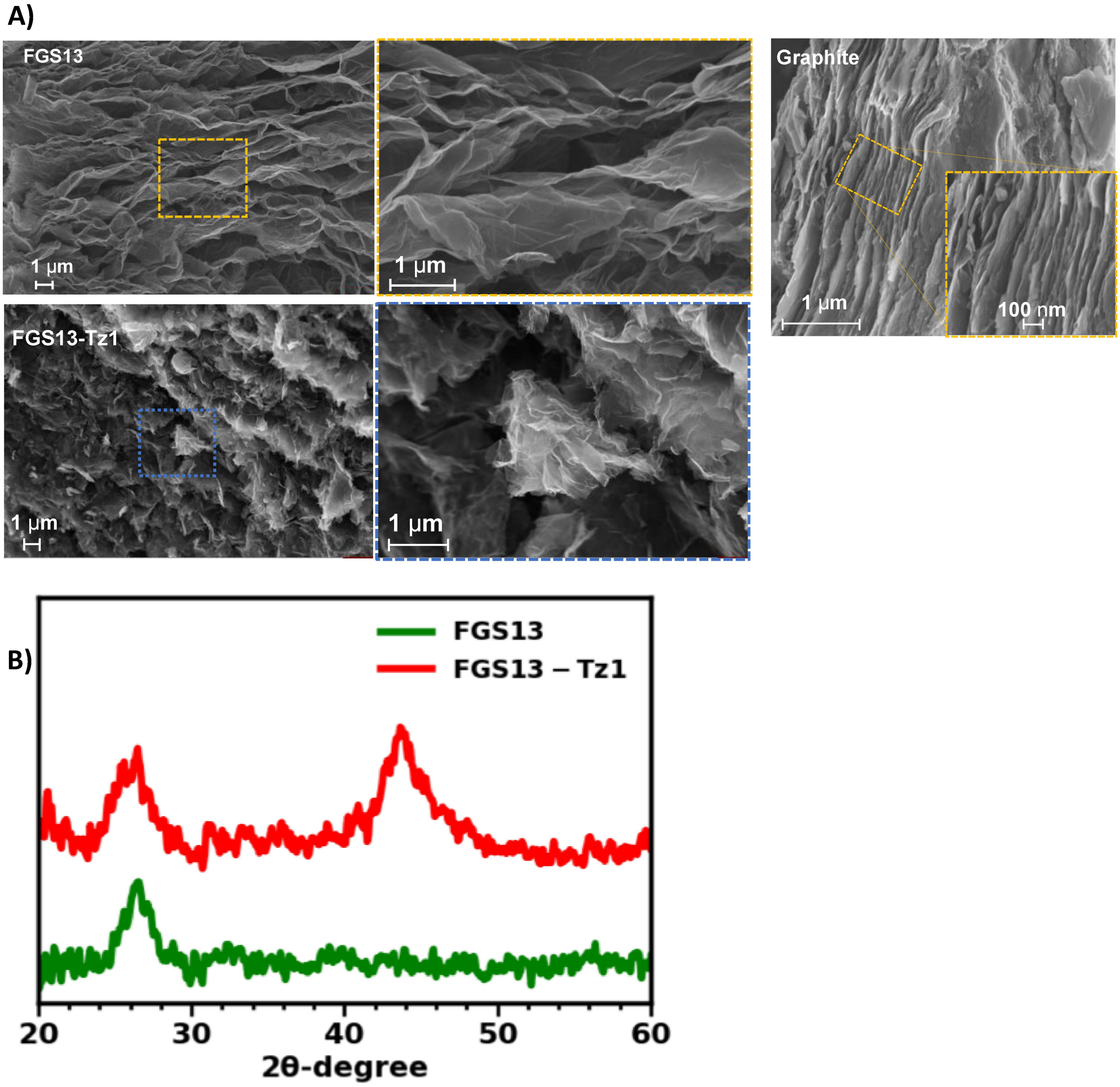

Figure 7. SEM micrographs (A) and XRD patterns (B) of **FGS13** (top in A) and green line in B)) and **FGS13-Tz1** (bottom in A) and red line in B)). The 2θ values are reported regarding the Cu Kα radiation for ease of comparison with literature.

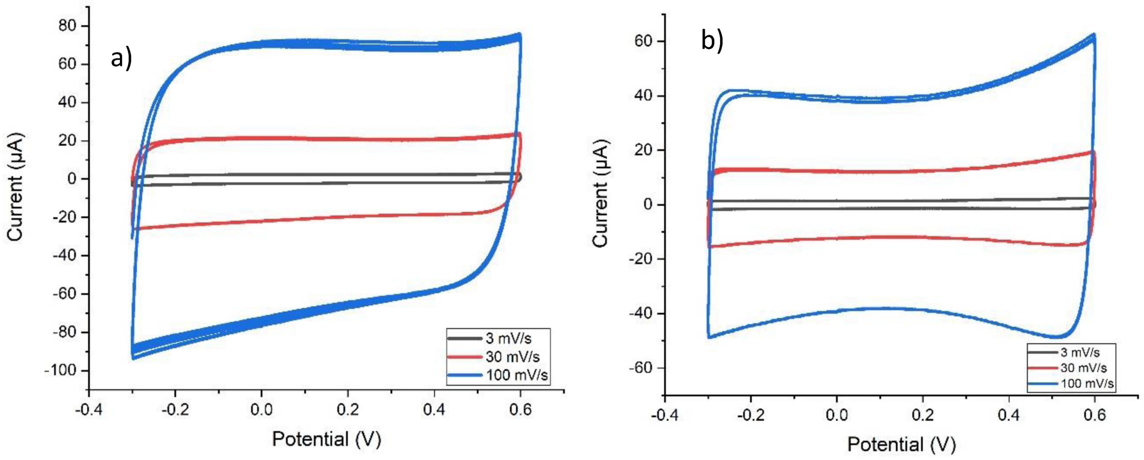

Figure 8. Typical cyclic voltammograms of **FGS13-Tz1** (a) and **FGS13-Tz2** (b) between −0.3 V and 0.6 V (in acetonitrile + TBAPF$_6$) vs. Ag$^+$/Ag at various scan rates. Mass of active material: 30 µg.

experimental section for protocol details). The results are displayed in Figure 9.

The capacitance of the material is evaluated from the CV curve according to Eq. 3:

$$C_m = \frac{1}{vm(U_2 - U_1)} \int_{V_1}^{V_2} I(V)dV \tag{3}$$

where, C_m is the specific capacitance in F/g, v is the scan rate (V/s), dV is the potential window, m is the active material mass, and the integral is the area of the CV curve.

The electrochemical response at low scan rates reveals interesting features when comparing **FGS13-Tz1** to pristine **FGS13**. First, a remarkable increase in the CV area can be seen at 10 mV/s which can be assigned to an increased specific area of the functionalized material. Then, at even lower scan rate (1 mV/s), the pseudocapacitive behaviour of **FGS13-Tz1** clearly appears in the upper limit of the electrochemical window (1.8–2.5 V) with an enhanced reduction peak due to the tetrazine moieties. This pseudocapacitance contribution of **Tz1** at high voltage accounts for 5% of the total capacitance, based on the relative integrations of CVs in Figure 9A. In the scan rate range between 20 and 100 mV/s, CVs with rectangular shapes typical of pure capacitive behaviour are obtained. The specific capacitance values for **FGS13-Tz1** extracted from these CVs are equal to 42.7, 38.7 and 32.3 F/g at respectively 20, 50 and 100 mV/s. These values are higher than those previously reported for tetrazine functionalized graphene in two electrode cells (typically 30 F/g at 20 mV/s)[15].

Galvanostatic charge discharge (GCD) at various current densities have been also used to determine the specific capacitance values using Eq. 4:

$$C_m = \frac{4I\Delta t}{m\Delta V} \tag{4}$$

Where I is the applied current, m is the mass of active material, ΔV is the potential range and Δt the discharge time.

The results are shown in Figure 10 and confirm that **FGS13-Tz1** displays significantly higher capacitance values than pristine graphene up to a current density of 2 A/g where both values tend to equalize.

A similar study was performed on **FGS13-Tz2** and the results are shown in figures S8-S9. Typically, the CV curve of **FGS13-Tz2** exhibits a nearly rectangular shape indicative of a pure capacitive behavior, except at 100 mV/s, where a deviation is observed. As expected, **FGS13-Tz2** was found to have a smaller capacitance than **FGS13-Tz1**, due to the bridging effect in the latter which enhances the charge storage ability by opening the inner nanostructuration, thus enhancing the specific area. This results in a smaller charge transfer resistance for **FGS13-Tz1** vs. both **FGS13** and **FGS13-Tz2** (typically 12 Ω vs. 18 and 38 Ω respectively measured by EIS) (Figure S10).

Finally, cycling studies over 1500 or 3000 cycles have been performed at a current density of 0.1 A/g (Figures S11–S12).

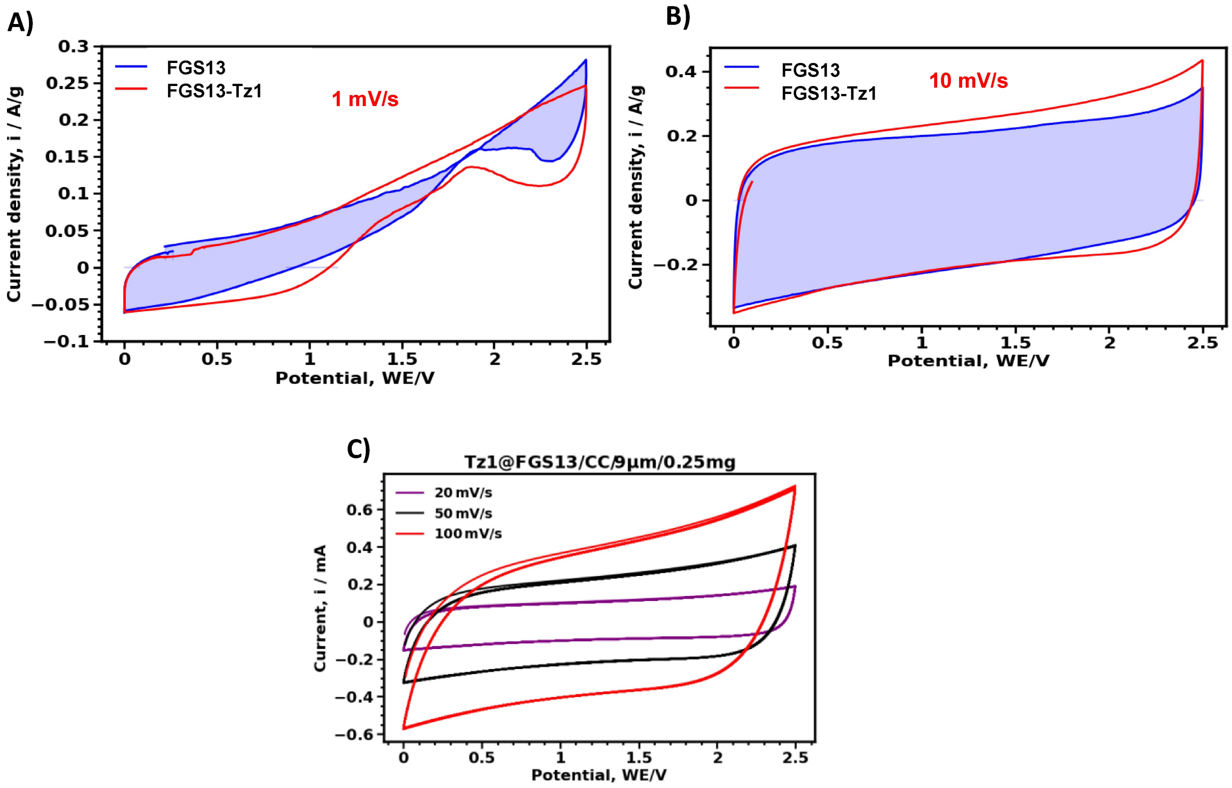

Figure 9. Cyclic voltammetries recorded in two-electrode Swagelok cells for FGS13 (blue) and FGS13-Tz1 (red) at 1 mV/s (A), 10 mV/s (B). CV of FGS13-Tz1 at various scan rates from 20 to 100 mV/s (C).

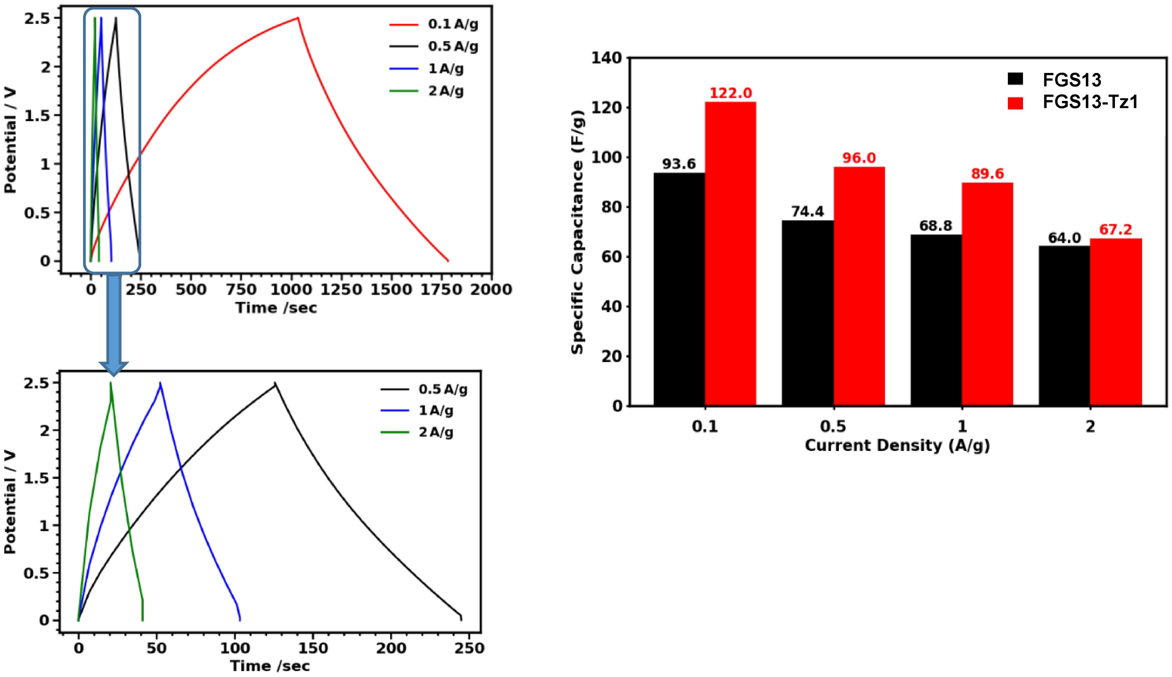

Figure 10. Galvanic Charge-Discharge curves of FGS13-Tz1 with a specific zoom on the high current densities and specific capacitance values for FGS13 and FGS13-Tz1 in two-electrode Swagelok cells.

Interestingly the results reveal that **FGS13-Tz1** is very stable along cycling with an excellent capacity retention when the potential window is limited to 1 V (Figure S12). In contrast, when the potential window is increased to 2.5 V, the capacity retention decreases to ~60 % after 3000 cycles (Figure S11). To understand the reason of this capacity drop, EIS was conducted after the 3000th cycle (Figure S11D) and revealed a high charge transfer resistance of approximately 3000 Ω for the largest potential window. When the potential range is limited to 1 V, analysis of the EIS data (Figure S12 C) shows an increase in the RC circuit elements after each 50 cycles. Notably, the charge transfer resistance exhibited approximately a 68 % increase after 500 cycles. Similarly, the Warburg diffusion element displayed a comparable (59 %) increase (Figure S12D). However, despite these increases, the charge storage ability of the electrode remained unaffected, as a capacity loss of less than 10 % was recorded after 1500 cycles.

The performance difference between both potential windows is also visible when comparing the coulombic efficiencies, expressed as the discharge vs. charge capacity ratios. Figure 11 clearly displays that the coulombic efficiency remains limited to ca. 65 % for 2.5 V whereas it reaches 95 % at 1 V, both remaining constant upon cycling after 300 cycles. We can postulate that the limited performance at 2.5 V is related to the electrolyte

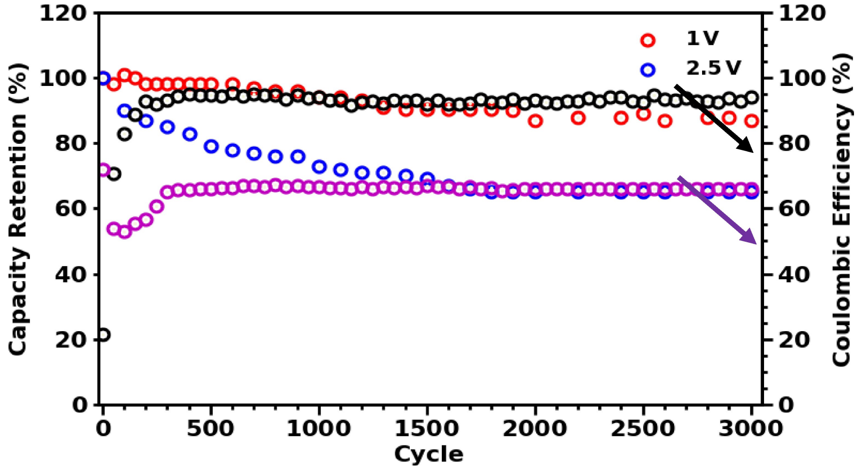

Figure 11. Plot of the capacity and coulombic efficiency of **FGS13-Tz1** at 1 V (red and black) and 2.5 V (blue and purple). The arrow is pointing the data to the coulombic efficiency axis.

composition and that another choice of ions and solvent might improve significantly the results.

Conclusions

A new molecule bearing two tetrazine anchoring groups and a tetrazine redox unit was synthesized and successfully grafted on reduced graphene oxide by inverse demand Diels-Alder reaction. Elemental analysis and XPS were used to assess the molar fraction of tetrazine in the final material. Cyclic voltammetry demonstrates that the electroactivity of the central tetrazine is preserved in the material, while Raman spectroscopy, AFM and XRD have shown that the initial aim of making some bridges between graphene sheets has been at least partially achieved. The capacitance of the functionalized graphene was measured first in a three electrode cell, displaying a significant increase compared to both the pristine graphene and a model functionalized graphene without bridging possibilities. This increase is confirmed in two electrode capacitors with a 30% increase up to 1 A/g. These results demonstrate the interest of opening the graphene structure to develop the specific area while incorporating a redox unit at the same time. This leads to a final material with energy storage ability through joined capacitive and faradaic effects.

Experimental section

Synthesis

All commercial reagents were used as received. The solvents were dried by conventional methods. Column chromatography was performed using a Combiflash. The reactions were monitored by TLC on a silica gel plate and visualized by UV light. The ^{1}H NMR and ^{13}C NMR spectra were recorded on a JEOL ECS 400 MHz spectrometer.

Elemental analysis

Elemental analysis was conducted on a Flash EA1112 Thermo Finigan analyser driven with a Eager Xperience software. The samples are preliminary heated at 970 °C. Analysis is conducted with He as vector gas with a rate of 140 mL/min.

XPS

XPS measurements were performed using a K-Alpha^{+} spectrometer (ThermoFisher Scientific, East Grinstead, UK) operated in the constant analyzer energy mode, and equipped with a micro-focused and monochromatic Al Kα X-ray source (1486.6 eV, spot size: 400 μm, 12 kV, 6 mA) and a flood gun (for insulating samples). The samples were clipped onto the sample holder and outgassed overnight in the fast-entry lock. The step size and pass energy were set to 1 eV/200 eV and 0.1 eV/40 eV for the survey and the high resolution regions, respectively. Data acquisition and processing was done using Avantage software (ThermoFisher Scientific), version 5.9902. The surface chemical composition was determined by using the manufacturer sensitivity factors.

AFM

AFM images were collected on a Icon Dimension Atomic Force Micrsocope (Bruker) equiped with Si PointProbePlus tips (**PPP-NCHR, NanoSensors**) operated on tapping mode. The samples were prepared by dropcasting suspensions of 0.1 mg/mL graphene flakes over a Si wafer.

Raman Spectroscopy

Raman microscopy experiments were conducted in a TiU2 Inverted microscope (Nikon). The excitation laser beam ($\lambda = 633$ nm) is spatially filtered using a 50 μm pinhole and spectrally cleaned with the help of a bandpass filter (633/5, Chroma) before being introduced into the microscope through the backport. The light is focused on the sample on a ~1 μm zone with the help of an extra long working distance 40× objective (0.6 NA, Nikon), which also collects the scattered light. Rayleigh scattering is separated from the Raman signal with the help of a dichroic mirror (RazorEdge LP02 633RU −25, Semrock) and a Long pass filter (LPD02 633RU-25, Semrock), before being injected into the spectrometer (Jobin Yvon, HR400) equipped with a 300 mm^{-1} grating and a N_2 cooled CCD sensor.

Samples were prepared by drop casting disperse graphene 1 mg/mL dichlorometane suspensions over coverslips.

SEM

SEM was performed on a ZEISS Ultra 55 scanning electron microscope equipped with a field emission gun to efficiently extract electrons for high-resolution imaging. The microscope's secondary electron detectors were used for observations. Tungsten filament coated with zirconium oxide was used to emit electrons from the tip and the SEM operates at an acceleration voltage of 3.00 kV with a working distance between 4 mm and 8 mm.

XRD

XRD measurements were performed at the LAPA Laboratory in CEA of Saclay, using a photon microprobe built on a Rigaku RU200 rotating anode X-ray generator running at 55 kV and 21 mA. The beam delivered by a molybdenum anode (Kα~17.45 keV–0.70932 Å) was monochromatized using a FOX-2D (Xénocs) toroidal multilayer mirror and then focused on a surface of 100×100 μm^2 with an average flux of 20×10^6 ph/s. Diffracted patterns were recorded using a RebirX-70S (Cegitek, Aubagne, France) hybrid pixel array detector. Data processing was carried out with the EVA software (Bruker AXS) and the ICDD-JCPDS database.

Electrode preparation for capacitance measurements

In three-electrode cells, electrodes were prepared according to a procedure published by Dong:[31] a certain amount of graphene was dispersed in N-methyl-2-pyrrolidone (NMP) by ultrasonication for 1 hour. Then, 30% PVDF was added to the dispersion as a binder and the mixture was heated for 3 hours at 60 °C. Then, the mixture was deposited by drop-casting on a glassy carbon electrode and was heated at 100 °C to eliminate the solvent.

For capacitance measurements in Swagelok cells, the electrode preparation was the following: the active material (10 mg) and conductive carbon (1.25 mg) were initially grounded manually for a period of 10 minutes. This mixture was then added to PVDF (1.25 mg) which had been previously dissolved in NMP (6 drops).

Subsequently, 10–15 additional drops of NMP were added to the mixture, and the grinding process was continued for a further 20 minutes to obtain a homogenous ink. The final composite material contained 80 wt.% of the active material.

The prepared ink was then deposited onto an aluminum substrate using Doctor Blade equipment and allowed to dry overnight at ambient room temperature. Once dry, the electrodes were cut into disks of 9 mm diameter and pressed with a force of 1 ton to enhance their mechanical properties and material contact with the current collector. The electrodes were subsequently dried under vacuum in a Buchi oven at 100 °C for 4 h to completely evaporate NMP solvent. After drying, the electrodes were weighed to determine the mass of the active material. In addition, the thickness of the electrodes was measured using a micrometer. The mass and thickness of the active material were found to be in the ranges of 0.25–0.4 mg and 10–20 μm, respectively. These precise measurements ensured that the electrodes were of high quality and suitable for use in electrochemical measurements.

The different steps are summarized in the Scheme 3:

Cell assembly

The electrodes were carefully prepared and assembled within a 2-electrode symmetric Swagelok cell. A glass fiber separator with a diameter of 16 mm, was used and soaked with 300 μL of electrolyte consisting of $TBAPF_6$ 1.5 M in ACN, which was previously bubbled under Argon.

All cell assembly procedures were carefully carried out under ambient room temperature conditions. To ensure accurate electrical contact within the cell, the open circuit voltage was measured and confirmed to be close to 0 V. The cells were then left undisturbed for a period of 12 hours to ensure optimal stability before any electrochemical measurements were conducted.

Electrochemistry

3-electrode cell

Cyclic voltammetry was performed with a CHI 600 potentiostat with ITO plates (Solems, 25×25 mm) as working electrodes, a platinum wire as a counter electrode and an Ag/AgCl reference electrode.

2-electrode Swagelok cell

Cyclic voltammetry (CV), galvanostatic charge-discharge (GCD), and electrochemical impedance spectroscopy (EIS) was performed with an EC-Lab VMP3 potentiostat. CV was undertaken at scan rates ranging from 1 to 100 mV/s within a potential range of 0 to 2.5 V, corresponding to the standard organic electrolyte ($TBAPF_6$ 1.5 M in ACN). For GCD, the measurements were taken at a current density ranging from 0.1 to 2 A/g, with a maximum and minimum potential of 0 and 2.5 V, respectively. Finally, EIS experiments were conducted at a frequency range from 100 mHz to 200 KHz.

Author Contributions

MB did the experiments of functionalization and characterization. AA did the electrochemical measurements in two-electrode cells and XRD, SEM characterizations. EM synthesized the molecules. AB supervised the AFM experiments. VB supervised the Raman experiments. PA had the idea of the molecules and supervised their synthesis. RP and MG supervised AA's work and participated to the writing of the manuscript. FM supervised MB's work and wrote the main part of the manuscript.

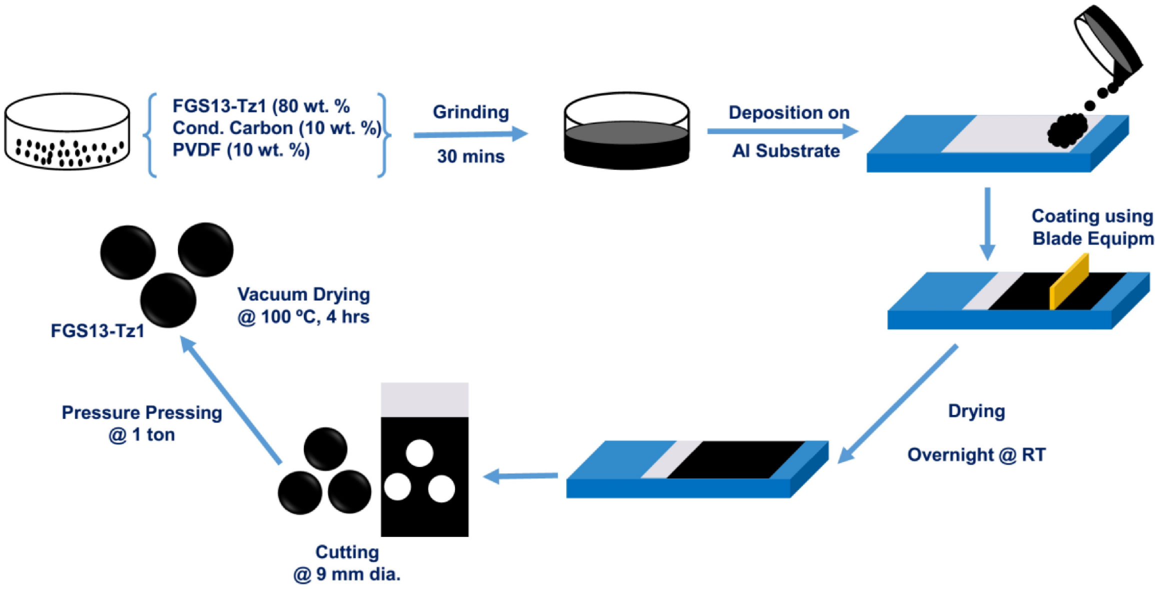

Scheme 3. Experimental procedure for electrode preparation in Swagelok cells.

Acknowledgements

Elemental analysis was performed by G. Excoffier (Service d'analyses, Spectropole, Faculté des sciences de l'Université de Marseille). **FGS 13** was gently provided by I. Aksay (Princeton University). XPS was performed by P. Decorse (ITODYS, Université Paris-Cité). We are grateful to Eddy Foy (LAPA-IRAMAT, CEA Saclay) for performing the XRD measurements. The RebirX-70S detector for XRD measurement was supported financially by the Paris Ile-de-France Region DIM "Matériaux anciens et patrimoniaux". We thank the Institute for Sustainable Energy (Université Paris-Saclay) for funding Ademola Adeniji's internship.

Conflict of Interests

The authors declare no conflict of interest.

Data Availability Statement

The data that support the findings of this study are available from the corresponding author upon reasonable request.

Keywords: Graphene · electrochemical storage · supercapacitors · tetrazine

[1] A. K. Geim, K. S. Novoselov, *Nat. Mater.* **2007**, *6*, 183–191.
[2] S. Stankovich, D. A. Dikin, G. H. B. Dommett, K. M. Kohlhaas, E. J. Zimney, E. A. Stach, R. Piner, D. S. T. Nguyen, R. S. Ruoff, *Nature* **2006**, *442*, 282–286.
[3] G. Kucinskis, G. Bajars, J. Kleperis, *J. Power Sources* **2013**, *240*, 66–79.
[4] A. G. Olabi, M. A. Abdelkareem, T. Wilberforce, E. T. Sayed, *Renewable Sustainable Energy Rev.* **2021**, *135*, 110026.
[5] M. Pumera, *Energy Environ. Sci.* **2011**, *4*, 668–674.
[6] V. Georgakilas, M. Otyepka, A. B. Bourlinos, V. Chandra, N. Kim, K. C. Kemp, P. Hobza, R. Zboril, K. S. Kim, *Chem. Rev.* **2012**, *112*, 6156–6214.
[7] J. Park, M. Yan, *Acc. Chem. Res.* **2013**, *46*, 181–189.
[8] M. Quintana, K. Spyrou, M. Grzelczak, W. R. Browne, P. Rudolf, M. Prato, *ACS Nano* **2010**, *4*, 3527–3533.
[9] J. Li, M. Li, L.-L. Zhou, S.-Y. Lang, H.-Y. Lu, D. Wang, C.-F. Chen, L.-J. Wan, Click *J. Am. Chem. Soc.* **2016**, *138*, 7448–7451.
[10] G. Clavier, P. Audebert, *Chem. Rev.* **2010**, *110*, 3299–3314.
[11] Y. Li, F. Miomandre, G. Clavier, L. Galmiche, V. Alain-Rizzo, P. Audebert, *ChemElectroChem* **2017**, *4*, 430–435.
[12] J. Zhu, Hiltz, J. R. B. Lennox, R. Schirrmacher, *Chem. Commun.* **2013**, *49*, 10275–10277.
[13] M. L. Blackman, M. Royzen, J. M. Fox, *J. Am. Chem. Soc.* **2008**, *130*, 13518–19.
[14] N. K. Devaraj, R. Weissleder, *Acc. Chem. Res.* **2011**, *44*, 816–827.
[15] Y. Li, G. Louarn, P.-H. Aubert, V. Alain-Rizzo, L. Galmiche, P. Audebert, F. Miomandre, *Carbon* **2016**, *105*, 510–520.
[16] Y. Bin Rus, L. Galmiche, P. Audebert, A. Courty, E. Maisonhaute, F. Miomandre, *ChemistrySelect* **2019**, *4*, 1298–1305.
[17] J. Amaro-Gahete, A. M. Kaczmarek, D. Esquivel, C. Jimenez-Sanchidrian, P. Van Der Voort, F. J. Romero-Salguero, *Chem. Eur. J.* **2019**, *25*, 6823–6830.
[18] K. Pirnat, J. Bitenc, I. Jerman, R. Dominko, B. Genorio, *ChemElectroChem* **2014**, *1*, 2131–2137.
[19] S. D. Cho, J. K. Im, H.-K. Kim, H. S. Kim, H. S. Park, *Chem. Commun.* **2012**, *48*, 6381–6383.
[20] R. Shi, C. Han, H. Duan, L. Xu, D. Zhou, H. Li, Li, J. F. Kang, B. Li, G. Wang, *Adv. Energy Mater.* **2018**, *8*, 1802088.
[21] L. Hou, C. Kong, Z. Hu, Y. Han, B. Wu, *J. Electroanal. Chem.* **2021**, *895*.
[22] L. Fan, Q. Zhang, K. Wang, F. Li, L. Niu, *J. Mater. Chem.* **2012**, *22*, 6165–6170.
[23] D. P. De Sousa, J. H. Yu, C. J. Miller, Y. Chang, C. J. McKenzie, T. D. Waite, *Langmuir* **2019**, *35*, 12339–12349.
[24] I.-M. Lazar, A. M. Rostas, P. S. Straub, E. Schleicher, S. Weber, R. Muelhaupt, *Macromol. Chem. Phys.* **2017**, *218* 1700050.
[25] E. Kibena, M. Marandi, V. Sammelselg, K. Tammeveski, B. B. E. Jensen, A. B. Mortensen, M. Lillethorup, M. Kongsfelt, S. U. Pedersen, K. Daasbjerg, *Electroanalysis* **2014**, *26*, 2619–2630.
[26] Z. P. Qiu, J. Yu, P. Yan, Z. J. Wang, Q. J. Wan, N. J. Yang, *ACS Appl. Mater. Interfaces* **2016**, *8*, 28291–28298.
[27] Y. B. Rus, Y. Qu, M. Bosmi, L. Galmiche, P. Audebert, F. Miomandre, *Mater. Chem. Phys.* **2022**, *291*, 126607.
[28] Y. Li, V. Alain-Rizzo, L. Galmiche, P. Audebert, F. Miomandre, G. Louarn, M. Bozlar, M. A. Pope, D. M. Dabbs, I. A. Aksay, *Chem. Mater.* **2015**, *27*, 4298–4310.
[29] W. Ai, X. Cao, Z. Sun, J. Jiang, Z. Du, L. Xie, Y. Wang, X. Wang, H. Zhang, W. Huang, T. Yu, *J. Mater. Chem. A* **2014**, *2*, 12924–12930.
[30] Y. Qu, F.-X. Sauvage, G. Clavier, F. Miomandre, P. Audebert, *Angew. Chem. Int. Ed.* **2018**, *57*, 12057–12061.
[31] J. Dong, Z. Wang, X. Kang, *Colloids Surf. Physicochem. Eng. Asp.* **2016**, *489*, 282–288.
[32] F. T. Johra, J.-W. Lee, W.-G. Jung, *J. Ind. Eng. Chem.* **2014**, *20*, 2883–2887.
[33] P. Audebert, F. Miomandre, G. Clavier, M. C. Vernieres, S. Badre, R. Meallet-Renault, *Chem. Eur. J.* **2005**, *11*, 5667–5673.
[34] M. S. Dresselhaus, A. Jorio, A. G. Filho Souza, R. Saito, *Philos. Trans. R. Soc. Math. Phys. Eng. Sci. 368* **2010**, *368*, 5355–5377.
[35] M. M. Lucchese, F. Stavale, E. H. Martins Ferreira, C. Vilani, M. V. O. Moutinho, Rodrigo B. Capaz, C. A. Achete, A. Jorio, *Carbon* **2010**, *48*, 1592–1597.
[36] J. H. Chen, W. G. Cullen, C. Jang, M. S. Fuhrer, E. D. Williams, *Phys. Rev. Lett.* **2009**, *102*, 236805.
[37] A. Jorio, M. M. Lucchese, F. Stavale, E. H. M. Ferreira, M. V. O. Moutinho, R. B. Capaz, C. A. Achete, *J. Phys. Condens. Matter* **2010**, *22*, 334204.
[38] H. Wang, Y. Wang, X. Cao, M. Feng, G. Lan, *J. Raman Spectrosc.* **2009**, *40*, 1791–1796.
[39] J.-B. Wu, M.-L. Lin, X. Cong, H.-N. Liu, P.-H. Tan, *Chem. Soc. Rev.* **2018**, *47*, 1822.
[40] L. M. Rivera, S. Fajardo, M. Del Carmen Adevalo, G. Garcia, E. Pastor *Catalysts* **2017**, *7*, 278.
[41] S. Li, W. Wang, X. Liu, X. Zeng, W. Li, N. Tsubaki, S. Yu, ***RSC Adv.*** **2016**, *6*, 13450–13455.

Manuscript received: September 12, 2023
Revised manuscript received: November 10, 2023
Version of record online: ■■, ■■

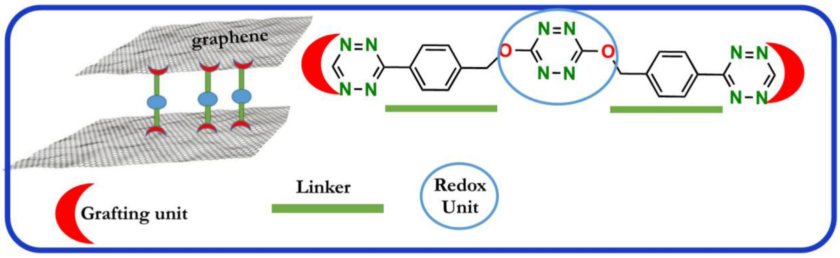

Supercapacitors: Functionalization of reduced graphene oxide sheets by redox-active bridging units leading to an enhanced capacitance and energy storage ability.

*Dr. M. Bosmi, A. Adeniji, E. Michel, A. Brosseau, Dr. V. Brasiliense, Prof. P. Audebert, Dr. R. Pongilat, Dr. M. Gauthier, Prof. F. Miomandre**

1 – 15

Functionalization and Crosslinking of Reduced Graphene Oxide Sheets by Multiple Tetrazine Units to Improve the Energy Storage in Supercapacitors